


Simultaneous Detection of Multiple Tumor-targeted Gold Nanoparticles in HER2-Positive Breast Tumors Using Optoacoustic Imaging

Abhilash Samykutty, PhD • Karl N. Thomas, BS • Molly McNally, MS • Jordan Hagood, BS • Akiko Chiba, MD • Alexandra Thomas, MD • Libby McWilliams, MS • Bahareh Behkam, PhD • Ying Zhan, PhD • McAlister Council-Troche, MS • Juan C. Claros-Sorto, MD • Christina Henson, MD • Tabitha Garwe, PhD • Zoona Sarwar, MS • William E. Grizzle, MD, PhD • Lacey R. McNally, PhD

From the Department of Surgery, Stephenson Comprehensive Cancer Center, University of Oklahoma, Oklahoma City, Okla (A.S., M.M., J.H., L.M., J.C.C.S.); Department of Radiation Oncology, University of Oklahoma Health Science Center, Oklahoma City, Okla (C.H.); Atrium Wake Forest Health Comprehensive Cancer Center, Winston-Salem, NC (A.T., L.M.); Department of Surgery, Duke University, Durham, NC (A.C.); Department of Cancer Biology, Wake Forest School of Medicine, Winston-Salem, NC 27013 (A.S., K.N.T., M.M., L.R.M.); Department of Mechanical Engineering, Virginia Tech University, Blacksburg, Va (B.B., Y.Z., M.C.T.); and Department of Epidemiology and Biostatistics (T.G., Z.S.) and Department of Pathology (W.E.G.), University of Alabama at Birmingham, Birmingham, Ala. Received December 19, 2022; revision requested February 22, 2023; revision received April 12; accepted April 26. **Address correspondence to** L.R.M. (email: lacey_mcnally@hotmail.com).

Supported in part by the National Cancer Institute (grant nos. R01CA205941, R01CA212350, P30CA225520, and U54CA118948), OUCARES, V. V. Cooke Foundation, and Williams Family Chair in Breast Oncology.

Conflicts of interest are listed at the end of this article.

Radiology: Imaging Cancer 2023; 5(3):e220180 • <https://doi.org/10.1148/rycan.220180> • Content codes: 

Purpose: To develop optoacoustic, spectrally distinct, actively targeted gold nanoparticle-based near-infrared probes (trastuzumab [TRA], TRA-Aurelia-1, and TRA-Aurelia-2) that can be individually identifiable at multispectral optoacoustic tomography (MSOT) of human epidermal growth factor receptor 2 (HER2)-positive breast tumors.

Materials and Methods: Gold nanoparticle-based near-infrared probes (Aurelia-1 and 2) that are optoacoustically active and spectrally distinct for simultaneous MSOT imaging were synthesized and conjugated to TRA to produce TRA-Aurelia-1 and 2. Freshly resected human HER2-positive ($n = 6$) and HER2-negative ($n = 6$) triple-negative breast cancer tumors were treated with TRA-Aurelia-1 and TRA-Aurelia-2 for 2 hours and imaged with MSOT. HER2-expressing DY36T2Q cells and HER2-negative MDA-MB-231 cells were implanted orthotopically into mice ($n = 5$). MSOT imaging was performed 6 hours following the injection, and the Friedman test was used for analysis.

Results: TRA-Aurelia-1 (absorption peak, 780 nm) and TRA-Aurelia-2 (absorption peak, 720 nm) were spectrally distinct. HER2-positive human breast tumors exhibited a significant increase in optoacoustic signal following TRA-Aurelia-1 (28.8-fold) or 2 (29.5-fold) ($P = .002$) treatment relative to HER2-negative tumors. Treatment with TRA-Aurelia-1 and 2 increased optoacoustic signals in DY36T2Q tumors relative to those in MDA-MB-231 controls (14.8-fold, $P < .001$; 20.8-fold, $P < .001$, respectively).

Conclusion: The study demonstrates that TRA-Aurelia 1 and 2 nanoparticles operate as a spectrally distinct HER2 breast tumor-targeted *in vivo* optoacoustic agent.

Supplemental material is available for this article.

© RSNA, 2023

Recent reports have shown that nearly 20% of patients who underwent breast conservation surgery required additional breast surgery due to the identification of residual cancer in margins, as described in the final pathology report. This demonstrates an originally false-negative intraoperative margin assessment (1–5). Accurate predictions of margin status are critical for guiding cancer surgery. However, currently available intraoperative margin assessment techniques are not sufficiently sensitive and cannot assess the receptor status of the tumor. Hence, in the clinical setting, novel approaches and technologies to improve intraoperative imaging-guided breast cancer surgery are needed. The major shortcoming of current breast-conserving therapy is the difficulty of distinguishing negative surgical margins of the tumor mass, which often leads to excision of a larger amount of normal breast tissue than necessary (6). Surgery is followed by radiation therapy to eradicate any

residual disease; however, radiation can also cause damage to the remaining healthy cells (7,8).

Multispectral optoacoustic tomography (MSOT) is a recently developed clinical optoacoustic technique that has the potential to overcome these limitations, as it is a reliable, nonionizing imaging method (9–14). MSOT combines deep-seated high-resolution imaging with multiwavelength illumination to simultaneously resolve and distinguish several extrinsically administered active, targeted contrast agents and endogenous absorbers (15–18). Delivery of tumor-specific contrast agents allows MSOT to depict and image multiple different cell populations or tumor markers concurrently (19–22). However, MSOT has not been fully explored to quantitatively characterize intratumor heterogeneity *in vivo*, partially due to a lack of tumor-specific probes.

A recently developed optoacoustic US system could successfully identify benign and malignant breast

Abbreviations

GNR = gold nanorod, HER2 = human epidermal growth factor receptor 2, ICP-MS = inductively coupled plasma mass spectrometry, MSOT = multispectral optoacoustic tomography, NIR = near-infrared, TNBC = triple-negative breast cancer, TRA = trastuzumab, WFBCCC = Wake Forest Baptist Comprehensive Cancer Center

Summary

The synthesized trastuzumab (TRA)-Aurelia-1 and TRA-Aurelia-2 was able to operate as a spectrally distinct, actively targeted exogenous near-infrared contrast agent that could simultaneously depict HER2-positive breast tumors with multispectral optoacoustic tomography.

Key Points

- Two nanoparticle reporters (Aurelia-1 and Aurelia-2) were developed with distinct optoacoustic spectra and separately distinguished using multispectral optoacoustic tomography.
- Orthotopically implanted human epidermal growth factor receptor 2 (HER2)-positive breast tumors in mice and freshly resected human HER2-positive breast tumors showed uptake of both trastuzumab-Aurelia-1 and 2, which could be detected simultaneously with multispectral optoacoustic tomography.
- Active targeting of Aurelia-1 and 2 gold nanorods with trastuzumab, the standard of care for treating HER2 breast cancer, combined with the clinical utility of multispectral optoacoustic tomography imaging paves the way for potential clinical translation with both potential diagnostic and therapeutic implications.

Keywords

Molecular Imaging, Nanoparticles, Photoacoustic Imaging, Breast Cancer

disease using an endogenous single-excitation wavelength at near-infrared (NIR) spectra (13,23,24). However, such systems have drawbacks when using intrinsic probes: (a) melanin exhibits a discernible spectrum in the NIR region, but the process of spectral unmixing these distinct spectra isolated from the defined endogenous absorbers may lead to false-positive results (25,26), and (b) passive targeting or the detection of endogenous spectra in the heterogeneous tumor may provide false information in identifying the negative tumor margins (27,28).

Advances in nanotechnology have led to the development of multispectral NIR fluorophores for use in noninvasive biomedical imaging research (29). The multispectral ability of nanoprobe provides several unique images at greater tissue depths, allowing the simultaneous detection and monitoring of multiple disease status markers (eg, patterns of oxygenation, vascularization, and metastasis) throughout an entire tumor. Currently, the handheld MSOT system, Acuity (iThera Medical), has shown promising applications in delineating benign and malignant breast lesions that can potentially improve clinical detection of breast cancers (13,14).

The nanoparticle-based NIR probes (650–900 nm) recently gained widespread attention due to their favorable features as compared with other small organic chromophores. The NIR probes synthesized from gold nanorods (GNRs) have substantial advantages over other probe types:

multispectral capability, enhanced plasmon resonance, higher resolution, and increased sensitivity. GNRs synthesized at the visible and NIR spectral window emit light that can penetrate up to 5 cm into tissues with minimal absorption and scattering (30). Due to the combination of several unique features such as thermal properties, optical properties, and tunable size, shape, and surface chemistry, gold has been used in clinical trials for advanced-stage solid organ cancers, coronary atherosclerosis, and rheumatoid arthritis (31–33).

In the current study, two viable spectrally distinct GNR-based NIR probes, Aurelia-1 and Aurelia-2, were synthesized. These probes were bioconjugated with trastuzumab (TRA), a human epidermal growth factor receptor 2 (HER2)-positive specific monoclonal antibody currently approved to treat breast cancers. This was done to make the probes HER2-specific for simultaneous visualization of multiple exogenous contrast agents. These active-targeted spectrally distinct exogenous NIR probes will enable optoacoustic concurrent imaging in HER2-positive cell populations that would not otherwise produce optoacoustic signals, thus potentially extending the use of MSOT for in vivo monitoring of distinct spectra for simultaneous imaging to identify HER2-positive tumors and improve image-guided surgery.

Materials and Methods

The Wake Forest Baptist Comprehensive Cancer Center (WFBCCC) institutional review board (protocol no. IRB00047646) approved human breast tumor sample collection following informed consent. The de-identified clinical information used in this study is in accordance with the WFBCCC ethics approvals. All animal experiments were performed in compliance with an approved Institutional Animal Care and Use Committee protocol of WFBCCC (protocol no. A17–014).

Generation of Spectrally Distinct TRA-Aurelia-1 and TRA-Aurelia-2 GNRs for Optoacoustic Imaging

Synthesis of Aurelia-1 and 2 was conducted via the seed-mediated method (19,34,35). Aurelia-2 synthesis was conducted as described previously, with minor modifications (34). The synthesized Aurelia-1 and 2 were conjugated with silica and chitosan on their surfaces (19) to prevent thermal expansion and to maintain photostability. Particle sizes were determined by transmission electron microscopy (FEI Company) (36) (refer to Appendix S4 for details).

The silica- and chitosan-coated Aurelia-1 and Aurelia-2 GNRs were conjugated with TRA to develop TRA-Aurelia-1 and TRA-Aurelia-2 GNRs (19) (refer to Appendix S1 for details). The TRA-Aurelia-1 and 2 were characterized by dynamic light scattering (36) and attenuated total reflection Fourier transform infrared spectroscopy measurements (Spectrum 100 Series ATR-FT-IR; PerkinElmer) (35) (refer to Appendix S2 for details and Figure S1 for results). The synthesis and characterization of both TRA-Aurelia-1 and TRA-Aurelia-2 were repeated three times.

Toxicity Assay

The evaluation of potential toxicity of silica-GNR-only particles as well as silica-GNR-chitosan particles conjugated with

Aurelia-1 and Aurelia-2 based-GNRs was performed by neutral red assay (37,38) (refer to Appendix S3 for details).

Determination of HER2 Positivity in Breast Cancer Cells by Western Blotting

Approximately 50 µg each of protein from DY36T2Q, AU-565, SKBR3 (positive for HER2 receptor), and MDA-MB-231 (negative for HER2 receptor) cells were isolated, and the samples were dissolved in loading buffer (ATCC). Proteins were separated using a NuPage 4%–12% Bis-Tris gel (Invitrogen) and then transferred onto nitrocellulose membranes using iBlot (Life Technologies). The nitrocellulose membranes were probed with primary and secondary antibodies and were analyzed using LI-COR Odyssey (LI-COR Biosciences) (9) (refer to Appendix S5 for details).

In Vitro Simultaneous MSOT Imaging of TRA-Aurelia-1 and TRA-Aurelia-2 in Breast Cells and Human Breast Tissue

A total of 2.0×10^6 breast tumor cells (DY36T2Q, AU-565, and MDA-MB-231) were grown in six-well plates containing Dulbecco's modified Eagle's medium with 10% fetal bovine serum and 1% L-glutamine (37°C and 5% CO₂). The breast cancer cells were incubated for 2 hours with TRA-Aurelia-1 alone, TRA-Aurelia-2 alone, or in a combination containing an Aurelia-1 (150 µg/100 µL) and Aurelia-2 concentration (150 µg/100 µL), respectively. The cells were washed (three times) with the pH-specific phosphate-buffered saline containing 10% fetal bovine serum. The cells were scraped and pelleted by centrifugation (1500 rpm for 10 minutes). The uptake of TRA-Aurelia-1 and TRA-Aurelia-2 from the Aurelia-1 and Aurelia-2 GNRs was measured with MSOT. Tissue-mimicking phantoms were also prepared for MSOT analysis. The pelleted cells were added to the fixed cylindrical tissue, mimicking phantoms of 2-cm diameter. Phantoms were prepared using a 1.3% w/w agar gel (Sigma-Aldrich) made from distilled water containing an intralipid 20% emulsion (Sigma-Aldrich) for light diffusion (6% v/v), resulting in a gel presenting a reduced scattering coefficient. DY36T2Q, AU-565, and MDA-MB-231 breast tumor cells were treated with either TRA-Aurelia-1, TRA-Aurelia-2, or in a combination containing spectrally distinct Aurelia-1 or Aurelia-2 GNRs and were added to the cylindrical opening in the tissue phantoms. All phantoms containing the samples were evaluated using MSOT with multiple wavelengths (680, 710, 730, 740, 760, 760, 770, 780, 800, 850, and 900 nm), as previously described, using the absorbance of Aurelia-1 and Aurelia-2 (Figure S3) (19,39). The concentration of TRA-Aurelia-1 and TRA-Aurelia-2 in human breast tissues was determined by inductively coupled plasma mass spectrometry (ICP-MS) (refer to Appendix S6 for details).

In Vivo Simultaneous MSOT Imaging of TRA-Aurelia-1 and TRA-Aurelia-2 in Orthotopic Breast Tumors

Four-week-old female athymic mice were orthotopically implanted with 2.0×10^6 DY36T2Q and MDA-MB-231 breast cancer cells in 50 µL of media without fetal bovine serum

based on previously demonstrated protocols (18,40). The study was performed with strict adherence to the WFBCCC University Institutional Animal Care and Use Committee–approved protocol. A diet of 2920× alfalfa-free feed (Harlan Laboratories) was used to reduce the background noise. DY36T2Q and MDA-MB-231 breast cancer cells were suspended in a sterile tube containing Dulbecco's modified Eagle's medium (serum free). Using a 30-gauge needle, 2.0×10^6 DY36T2Q and MDA-MB-231 cells/10 µL were injected into the mammary fat pad. The mammary fat pad was disinfected with Betadine (Avrio Health) prior to and after the injection. Ten microliters of phosphate-buffered saline without cells were sham injected into two mice. The mice were returned to their cages with food and water ad libitum. Thirty days after orthotopic implantation, mice (five mice per group) containing DY36T2Q and MDA-MB-231 cells were intravenously injected with TRA-Aurelia-1 (150 µg/100 µL) and TRA-Aurelia-2 (150 µg/100 µL) GNRs. Six hours following the injection, mice were imaged with the MSOT In-Vision 512 TF (iThera Medical). MSOT imaging was performed as previously described (15).

MSOT Imaging

Both the treated and untreated mice, as well as HER2-positive human breast tumor and HER2-negative triple-negative breast cancer (TNBC) tumors, were evaluated at multiple wavelengths (680, 710, 730, 740, 760, 770, 780, 800, 850, and 900 nm), with 25 signal averages per wavelength and an acquisition time of 10 µsec per frame (22,39,41). The temperature of water within the instrument was maintained at 33°C. Imaging was initiated after the mice or human tissue was allowed to equilibrate within the instrument for 5 minutes. The raw data of the multispectral-analyzed samples were reconstructed with ViewMSOT software, version 3.8 (Ithera Medical). Using ViewMSOT software, wavelengths corresponding to the Aurelia-1 and Aurelia-2 base were reconstructed at a resolution of 75 µm. The multispectral processing was conducted using linear regression with ViewMSOT version 3.8. The region of interest mean intensity was plotted over the tumor, liver, and kidney (all using 3.5 mm² ellipse), and the settings were kept constant for all image sections obtained throughout the experiment. The signal intensity obtained from TRA-Aurelia-1 and TRA-Aurelia-2 GNRs containing Aurelia-1 and Aurelia-2 base at the mouse tumor, liver, and kidney, as well as human tumor and duct epithelial tissues, were represented in MSOT arbitrary units.

Statistical Analysis

In vitro, the Kruskal-Wallis test was used to compare the signal intensity for each treatment and assess significant differences between TRA-Aurelia-1 and TRA-Aurelia-2 GNRs in both HER2-positive and TNBC tumors using SAS software, version 9.3 (SAS Institute). In vivo, the MSOT values for treatment with TRA-Aurelia-1, TRA-Aurelia-2, or in combination were compared with a Friedman test using SAS version 9.3. Similarly, we correlated the active targeting efficacy of both TRA-Aurelia-1 and TRA-Aurelia-2 in both HER2-positive and

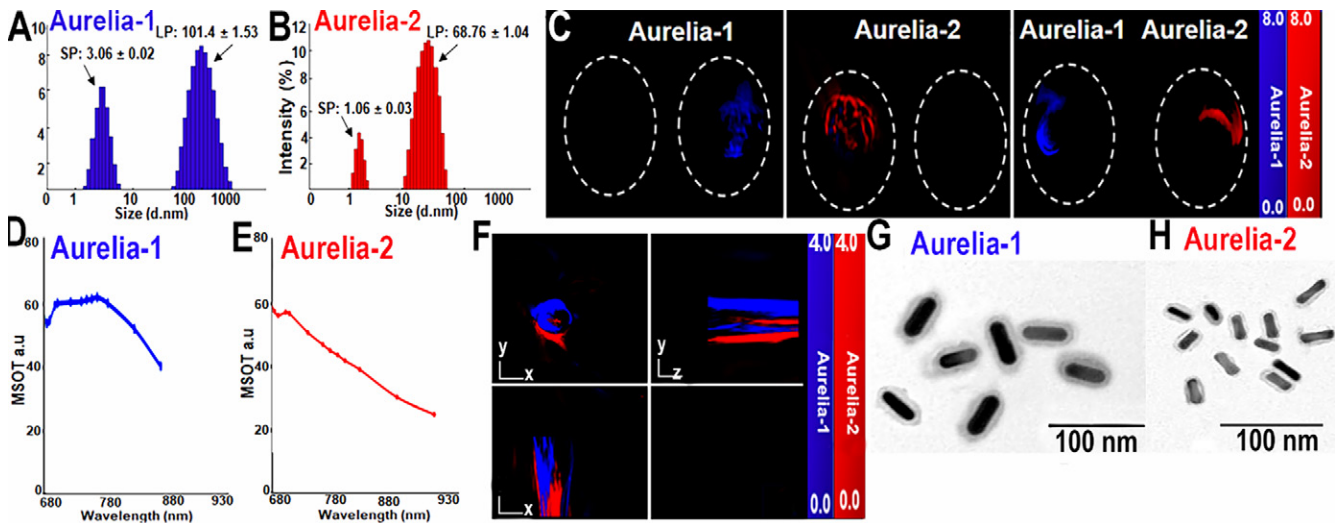


Figure 1: Characterization of spectrally distinct Aurelia-1 and Aurelia-2 gold nanorods (GNRs). **(A)** Dynamic light scattering–based distribution of Aurelia-1 (larger peak [LP], 101.4 ± 1.53 [SD]; polydispersity index [PDI], 0.82 ± 0.004) (smaller peak [SP], 3.06 ± 0.02 ; PDI, 0.82 ± 0.004). **(B)** Dynamic light scattering–based distribution of Aurelia-2 (LP, 68.76 ± 1.04 ; PDI, 0.82 ± 0.004) (SP, 1.06 ± 0.03 ; PDI, 0.82 ± 0.004). **(C)** Multispectral optoacoustic tomography (MSOT)–based detection of Aurelia-1 (blue) and Aurelia-2 (red) GNRs inside a tissue-mimicking phantom. **(D, E)** MSOT identification of the near-infrared spectral shape of Aurelia-1 (absorption peak at 780 nm) and Aurelia-2 (absorption peak at 720 nm). **(F)** MSOT detection of predefined blue (Aurelia-1) and red (Aurelia-2) color from the mixture of 1 mg of both GNRs after spectral unmixing. **(G, H)** Transmission electron microscopy image findings determined GNR size and total Aurelia-1 and Aurelia-2 size. Aurelia-1 and Aurelia-2 GNR sizes were as follows: Aurelia-1 length: $44.9 \text{ nm} \pm 2.01$, width: $35.75 \text{ nm} \pm 1.20$; Aurelia-2 length: $21.21 \text{ nm} \pm 2.12$, width: $9.13 \text{ nm} \pm 0.25$. The total particle sizes, including silica and chitosan, of Aurelia-1 and Aurelia-2 were as follows: Aurelia-1 length: $50.5 \text{ nm} \pm 3.06$, width: $38.92 \text{ nm} \pm 0.87$; Aurelia-2 length: $23.52 \text{ nm} \pm 2.09$, width: $10.23 \text{ nm} \pm 0.43$. a.u. = arbitrary units.

TNBC tumors using a Pearson correlation curve. *P* values less than .05 were sorted according to the correlation coefficient. A *P* value less than .05 was considered as statistically significant.

Results

Generation of Spectrally Distinct Aurelia-1 and 2 GNRs for MSOT Imaging

Using the seed-mediated approach, we synthesized two spectrally distinct gold nanoparticles. Aurelia-1 and Aurelia-2 were coated with mesoporous silica followed by a pH-sensitive chitosan gatekeeper to maintain optical absorption properties and tumor specificity of the probes in the acidic tumor microenvironment. The structural characterization of silica- and chitosan-conjugated Aurelia-1 (Fig 1A) and Aurelia-2 (Fig 1B) GNRs was determined by dynamic light scattering. The size of each GNR, as determined by transmission electron microscopy, was as follows: Aurelia-1 length: $44.9 \text{ nm} \pm 2.01$ (SD), width: $35.75 \text{ nm} \pm 1.20$; Aurelia-2 length: $21.21 \text{ nm} \pm 2.12$, width: $9.13 \text{ nm} \pm 0.25$ (Fig 1G, 1H). The total particle sizes, including silica and chitosan, of Aurelia-1 and Aurelia-2 were as follows: Aurelia-1 length: $50.5 \text{ nm} \pm 3.06$, width: $38.92 \text{ nm} \pm 0.87$; Aurelia-2 length: $23.52 \text{ nm} \pm 2.09$, width: $10.23 \text{ nm} \pm 0.43$ (Fig 1G, 1H). These nanoparticles were inserted into tissue-mimicking phantoms and imaged using MSOT to individually identify the distinct spectra of Aurelia-1 (Fig 1C, 1D) and Aurelia-2 (Fig 1C, 1E) gold nanoparticles in the NIR region (700–900 nm) that can be easily resolved from the endogenous contrast agents. Similarly, MSOT imaging of a mixture of Aurelia-1 and Aurelia-2 (Fig 1F) GNRs showed that each was individually detected

using the defined NIR spectra with linear regression spectral unmixing.

TRA-conjugated Aurelia-1- and 2-enhanced MSOT Imaging of HER2-expressing Breast Cancer Cells

Western blot analysis was used to determine the HER2 level in the various breast cancer cell lines. The HER2 receptor level protein expression was calculated for DY36T2Q (93 206 optical units, *P* = .002), SKBR3 (61 439 optical units, *P* = .019), AU-565 (57 100 optical units, *P* = .019), and MDA-MB-231 (5174 optical units) breast cancer cells. All three HER2-positive breast cancer cells (DY36T2Q, SKBR3, and AU-565) expressed higher levels of HER2 protein, and MDA-MB-231 cells were negative for HER2 receptors (Fig 2A, 2B; for full blot, refer to Figure S2). To initially evaluate the ability of the MSOT systems to correctly identify the TRA-Aurelia-1 and TRA-Aurelia-2 simultaneously at multispectral imaging, we first treated 2×10^6 DY36T2Q, SKBR3, and MDA-MB-231 cells with either TRA-Aurelia-1, TRA-Aurelia-2, or in combination for 2 hours under the pH of 7.4. All four cell lines were washed (phosphate-buffered saline pH, 7.4), scraped, and inserted into tissue-mimicking phantoms and imaged with MSOT. Following MSOT imaging, ViewMSOT software was used to analyze the best spectral fit corresponding to the TRA-Aurelia-1 (blue color) and TRA-Aurelia-2 (red color). Similarly, image processing for the combination treatment was able to simultaneously identify both TRA-Aurelia-1 and TRA-Aurelia-2 in HER2-positive DY36T2Q cells (TRA-Aurelia-1, *P* = .001; TRA-Aurelia-2, *P* = .001; combined TRA-Aurelia-1, *P* < .001; combined TRA-Aurelia-2, *P* = .003), SKBR3 (TRA-Aurelia-1, *P* = .006; TRA-Aurelia-2, *P* = .002; combined TRA-Aurelia-1,

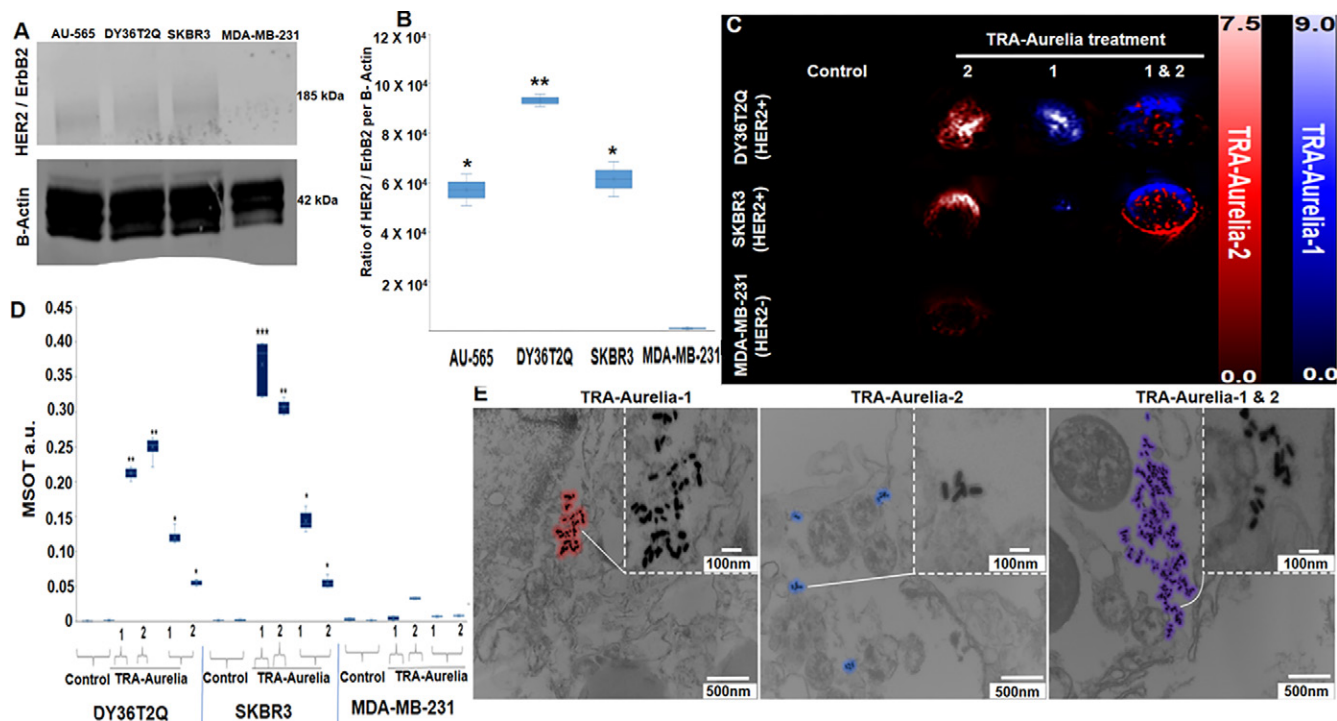


Figure 2: (A, B) Western blot analysis of human epidermal growth factor receptor 2 (HER2; also known as ERBB2)-positive expression profile in HER2-positive DY36T2Q (93 206 au, $P = .002$), SKBR3 (61 439 au, $P = .019$), AU-565 (57 100 au, $P = .019$), and HER2-negative MDA-MB-231 (5174 au) breast cancer cells. (C) DY36T2Q, SKBR3, and MDA-MB-231 cells after treatment with trastuzumab (TRA)-Aurelia-1 and TRA-Aurelia-2 were imaged with multispectral optoacoustic tomography (MSOT). Image postprocessing represents TRA-Aurelia-1 in blue and TRA-Aurelia-2 in red color. (D) Simultaneous MSOT-based detection of TRA-Aurelia-1 and TRA-Aurelia-2 in HER2-positive breast cancer cell lines DY36T2Q (TRA-Aurelia-1, $P = .001$; TRA-Aurelia-2, $P = .001$; combined TRA-Aurelia-1, $P < .001$; combined TRA-Aurelia-2, $P = .003$) and SKBR3 (TRA-Aurelia-1, $P = .006$; TRA-Aurelia-2, $P = .002$; combined TRA-Aurelia-1, $P < .001$; combined TRA-Aurelia-2, $P < .001$), in comparison with HER2-negative MDA-MB-231 cells. (E) Transmission electron micrograph demonstrates DY36T2Q cellular uptake of TRA-Aurelia-1 (outlined in blue), TRA-Aurelia-2 (outlined in red), and the combination of both (outlined in purple). TRA-Aurelia-1 and TRA-Aurelia-2 are distributed in the cytoplasm, vesicles, and nucleus. Individual TRA-Aurelia-1 and TRA-Aurelia-2 are shown in the inset. Transmission electron microscopy images of HER2-negative MDA-MB-231 cells did not show any uptake. *** = $P < .001$, ** = $P < .01$, and * = $P < .05$, a.u. = arbitrary units.

$P < .001$; combined TRA-Aurelia-2, $P < .001$) in comparison with the HER2-negative MDA-MB-231 cells (Fig 2C, 2D). The above results set a platform for simultaneous identification of the spectrally distinct TRA-Aurelia-1 and TRA-Aurelia-2 in the orthotopically implanted HER2-positive breast tumors. In vitro secondary confirmation of the simultaneous detection of TRA-Aurelia-1 and TRA-Aurelia-2 on the HER2-positive breast cancer cells were also evaluated by transmission electron microscopy imaging, which showed that TRA-Aurelia-1 and TRA-Aurelia-2 not deformed after being internalized inside the HER2-positive DY36T2Q cells via endocytosis (Fig 2E).

TRA-Aurelia-1 and 2-enhanced MSOT Signals from HER2-expressing Mouse Tumors

Athymic mice were orthotopically implanted with 2×10^5 breast cancer cells (DY36T2Q or MDA-MB-231) by mammary fat pad injection. Thirty days following implantation, the mice were separately or simultaneously tail-vein injected with equal amounts of TRA-Aurelia-1 and TRA-Aurelia-2. After 6 hours, significant accumulation of TRA-Aurelia-1 (blue, 14.8-fold increase, $P < .001$) and TRA-Aurelia-2 (red, 20.8-fold increase, $P < .001$) was observed via MSOT in mice implanted with HER2-positive DY36T2Q (Fig 3A, 3B) xenografts compared with HER2-negative MDA-MB-231 groups (Fig 3C,

3D). Mice injected with MDA-MB-231 orthotopic xenografts did not have any detectable signal at 6 hours. The smaller size of TRA-Aurelia-2 allowed for higher tumor penetration when compared with TRA-Aurelia-1. Thus, TRA-Aurelia-2 had higher accumulation in DY36T2Q tumors when both particles were injected simultaneously. Similar levels of breast tumor penetration were observed during individual injections. Secondary confirmation of both the GNRs in mice breast tumors and organs was determined by ICP-MS.

MSOT Imaging of TRA-Aurelia-1 and 2 in HER2-expressing Excised Human Breast Tumors

The fresh surgically resected human HER2-positive breast tumors ($n = 6$) and HER2-negative TNBC tumors ($n = 6$) from patients with breast cancer were treated with either TRA-Aurelia-1 (100 $\mu\text{g}/100 \mu\text{L}$), TRA-Aurelia-2 (100 $\mu\text{g}/100 \mu\text{L}$), or in combination (2 hours). MSOT imaging simultaneously identified the spectra of both TRA-Aurelia-1 (780 nm) and TRA-Aurelia-2 (720 nm) in HER2-positive breast tissue (Table). The HER2-positive breast tissue had significant uptake of both TRA-Aurelia-1 (mean, 19.25 ± 0.667 ; maximum, 1.2; minimum, 13.3) and TRA-Aurelia-2 (mean, 16.16 ± 4.793 ; maximum, 20.6; minimum, 10.7) compared with the HER2-negative TNBC tumors (Fig 4A, 4B) ($P = .002$).

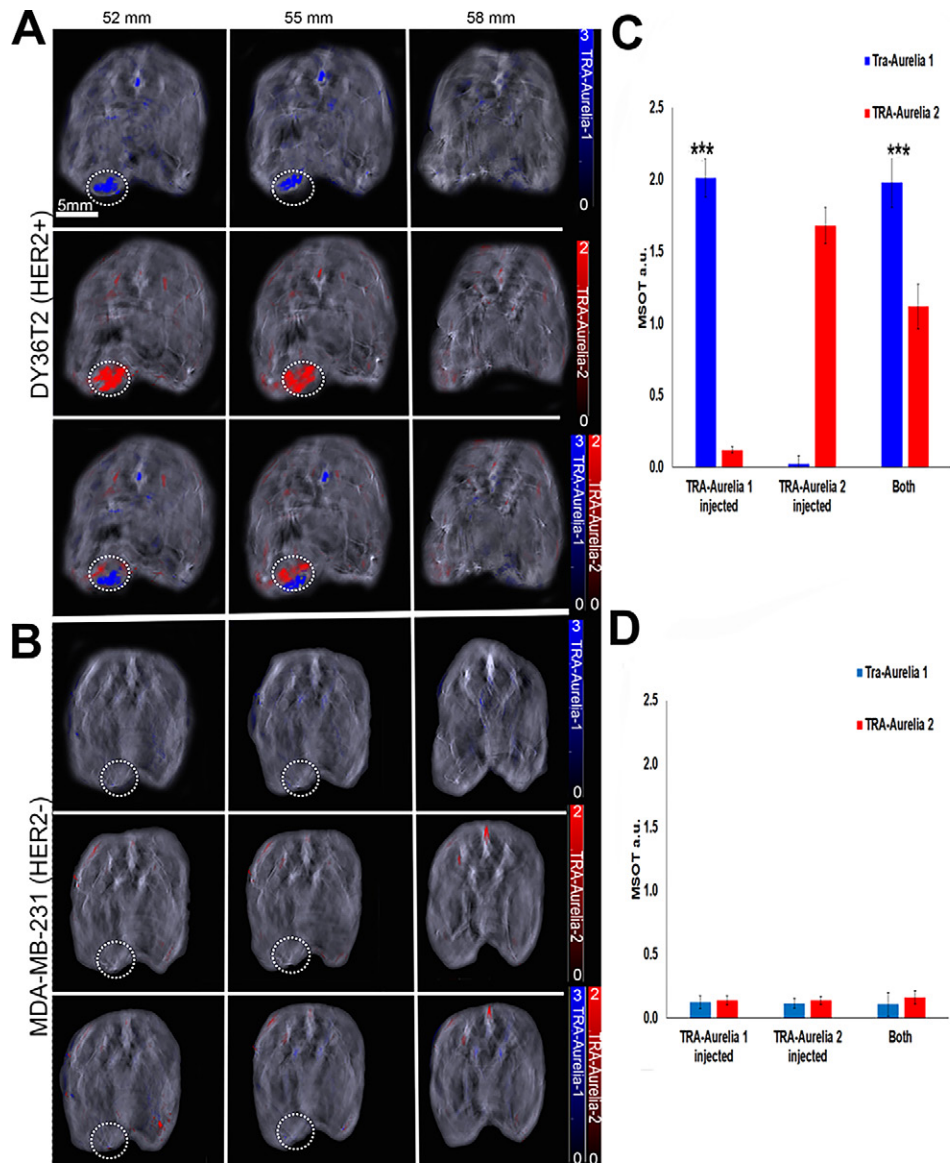


Figure 3: Simultaneous detection of the trastuzumab (TRA)-Aurelia-1 and Aurelia-2 gold nanorod (GNR) on images of athymic mice ($n = 5$; survival rate of 100%) bearing an orthotopically implanted mammary fat pad tumor (DY36T2Q or MDA-MB-231) at the predetermined time point of 6 hours after the intravenous injection of TRA-Aurelia-1 GNR, TRA-Aurelia-2 GNR, or in combination. **(A, B)** DY36T2Q breast tumor-bearing mice had high TRA-Aurelia-1 (blue color bar; 14.8-fold increase, $P < .0001$) and TRA-Aurelia-2 (red color bar; 20.8-fold increase, $P < .0001$) GNR uptake in the tumor in comparison with MDA-MB-231 tumor-bearing mice. **(C, D)** Bar graphs of multispectral optoacoustic tomography (MSOT) signal uptake in each cell line demonstrate that MDA-MB-231 breast tumor-bearing mice had negligible amounts of both TRA-Aurelia-1 and TRA-Aurelia-2 GNRs. *** = $P < .001$, a.u. = arbitrary units, HER2+ = human epidermal growth factor receptor 2-positive cells, HER2- = human epidermal growth factor receptor 2-negative cells.

The TNBC tumors had the lowest absorption of both TRA-Aurelia-1 (mean, 0.667 ± 0.339 ; maximum, 1.2; minimum, 0.3) and TRA-Aurelia-2 (mean, 0.548 ± 0.4 ; maximum, 1.3; minimum, 0.22) GNRs. We found a significant correlation between the active targeting efficacy of TRA-Aurelia-1 and TRA-Aurelia-2 ($r = 0.8$, $P = .002$) in the HER2-positive breast tumors (Fig 4C, 4D). Secondary confirmation of both GNRs in human breast tumor tissue was determined by ICP-MS analysis (Fig 5).

ICP-MS Analysis of TRA-Aurelia-1 and 2 in Mouse and Human Tumors

Athymic mouse models bearing DY36T2Q xenograft breast tumors were injected with both TRA-Aurelia-1 (150 $\mu\text{g}/100 \mu\text{L}$) and TRA-Aurelia-2 (150 $\mu\text{g}/100 \mu\text{L}$) via the tail vein. After 6 hours after injection, we euthanized the mice and collected the tumor, liver, kidney, and spleen. The organs underwent ICP-MS analysis for the determination of gold concentration. Similarly, surgically resected human tumor samples were

Ex Vivo Breast Tumor Tissue Information for Surgically Resected Samples Treated with TRA-Aurelia-1 and TRA-Aurelia-2

Patient	Subtype	Grade	Stage	Signal Intensity in Human Breast Tumor 2 Hours after Treatment ex Vivo at MSOT (au)	
				TRA-Aurelia-1	TRA-Aurelia-2
P1	HER2+	3	T2N0	19.4	14.7
P2	HER2+	3	T1cN0	16.6	10.9
P3	HER2+	3	T2N0	15.6	9.2
P4	HER2+	3	T1cN0	17.9	10.2
P5	HER2+	3	T1cN2	13.3	8.4
P6	HER2+	3	T2N0	18.7	8.11
P7	TNBC	3	T3N3a	0.2	0.1
P8	TNBC	3	T2N0	0.3	0.2
P9	TNBC	3	T4bN1a	0.5	0.2
P10	TNBC	3	T0N0	0.4	0.3
P11	TNBC	3	T2N1a	0.9	0.4
P12	TNBC	3	T1cN0	0.7	0.12

Note.—Data are represented in Figure 4A and 4D. au = arbitrary unit, HER2 = human epidermal growth factor receptor 2, MSOT = multispectral optoacoustic tomography, TRA = trastuzumab.

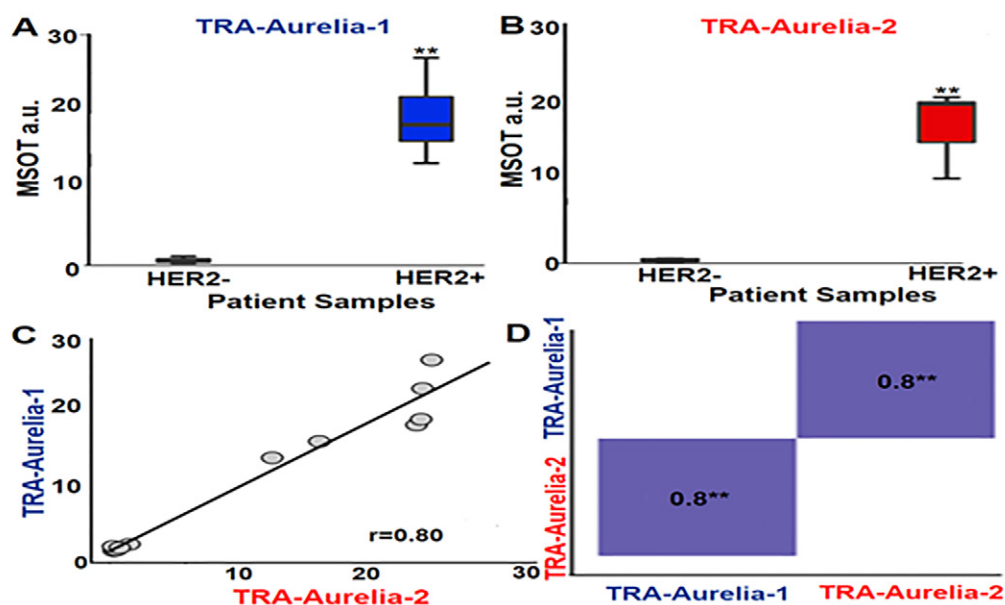


Figure 4: (A) Box plot shows a significantly higher trastuzumab (TRA)-Aurelia-1 uptake (mean, 19.25 ± 0.667 ; max, 1.2; min: 13.3) in human epidermal growth factor receptor 2 (HER2)-positive human breast tumors compared with HER2-negative tumors ($P = .002$ using Kruskal-Wallis test). (B) Box plot shows a significantly higher TRA-Aurelia-2 uptake (mean, 16.16 ± 4.793 ; max, 20.6; min, 10.7) in HER2-positive tumor tissue in comparison with HER2-negative tumors ($P = .002$ using Kruskal-Wallis test). Error bars describe 95% CI for each data point. (C, D) Pearson correlation curve data for TRA-Aurelia-1 and TRA-Aurelia-2 uptake in HER2 tumors shows significant correlation ($r = 0.8$, $P = .002$). ** = $P < .01$, a.u. = arbitrary units, MSOT = multispectral optoacoustic tomography.

treated with TRA-Aurelia-1 and TRA-Aurelia-2 for 2 hours and analyzed by ICP-MS to determine the gold concentration. Initially, the concentrations of the gold standard solution were translated to gold per gram of mouse tissue. A 100 $\mu\text{g}/\text{mL}$ solution of gold in 10% hydrochloric acid (v/v) was used as the stock solution to prepare the calibration standard solu-

tions in 2% (w/v) nitric acid + 0.5% hydrochloric acid (w/v) at concentrations of 0 (diluent blank), 0.1, 0.5, 1, 5, and 10 ng/mL . The concentrations in standard solution translated to approximately 0, 0.25, 1.25, 2.5, 12.5, and 25 μg gold per gram of mouse tissue, assuming a 20-mg sample size. The calibration curve was run once at the beginning of the assay, and multiple

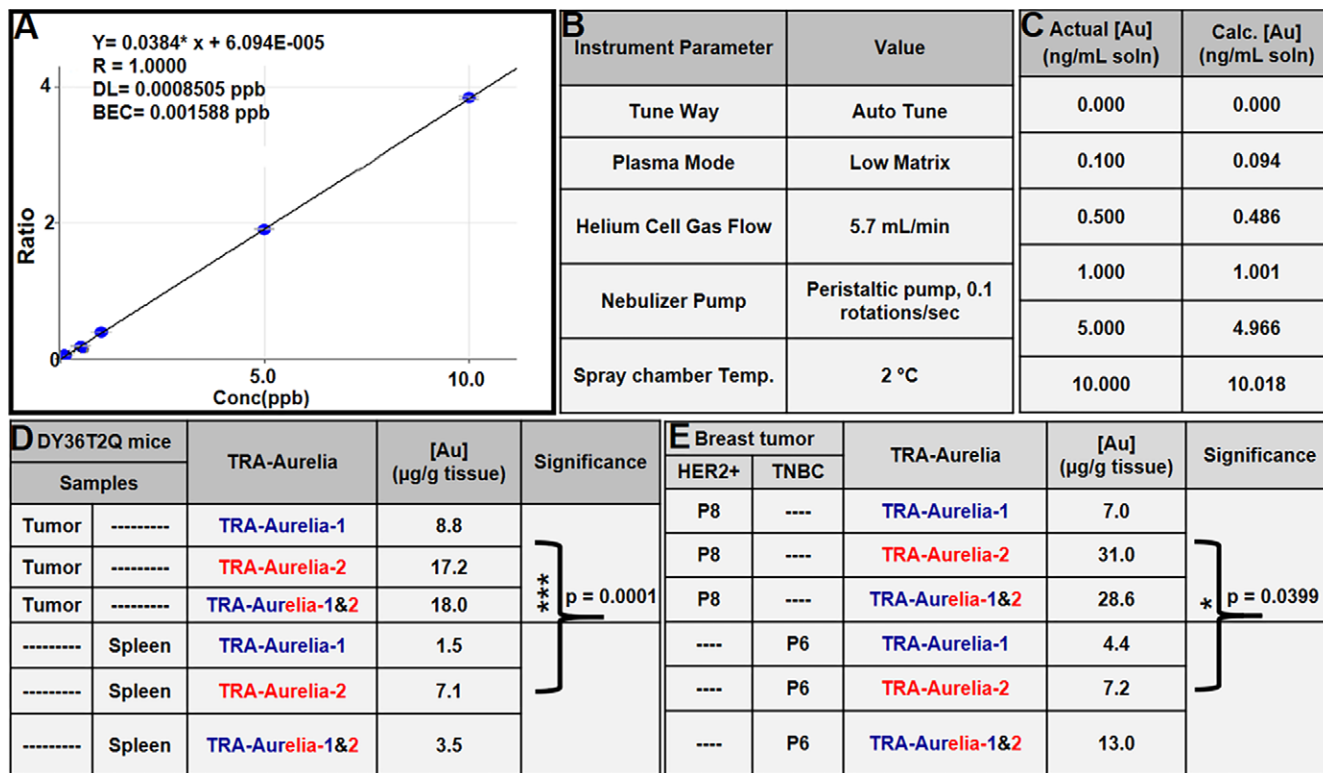


Figure 5: (A) Graph depicts a linear curve with various gold (Au) concentrations, translating into gold per gram of tissue, that confirms the presence of gold in mouse and human tissues. The 1000 µg/mL stock solution of platinum diluted to 0.4 µg/mL with 2% (w/v) nitric acid + 0.5% hydrochloric acid (w/v) is used as an internal standard. (B) Inductively coupled plasma mass spectrometry (ICP-MS) instrument parameters used in the gold analysis. (C) Comparison of the actual versus calculated gold concentrations observed during the ICP-MS analysis. (D) DY36T2Q breast tumors from mice had a gold content of 15 µg of gold per gram of tissue ($P < .001$) compared with 4 µg/g of gold observed in splenic tissue. (E) ICP-MS analysis of human epidermal growth factor receptor 2 (HER2)-positive human breast tumors indicated 22 µg of gold per gram of tissue ($P = .039$). *** = $P < .001$, * = $P < .05$, BEC = blank equivalent concentration, DL = detection limit, Temp = temperature, TRA = trastuzumab.

quality control standard solutions were run after the sample set to bracket the samples. Gold concentrations in this range used a diluent blank offset and produced a linear curve. The 1000 µg/mL stock solution of platinum in 5% nitric acid (v/v) was diluted to 0.4 µg/mL with 2% (w/v) nitric acid + 0.5% hydrochloric acid (w/v), and the dilute solution was used as the on-line addition internal standard (Fig 5A). ICP-MS analysis was performed with specific instrument parameters for gold analysis (Fig 5B). Both the actual and calculated gold concentrations were determined (Fig 5C). DY36T2Q xenograft mice breast tumors had 15 µg of gold per gram of tissue ($P < .0001$) compared with the 4 µg of gold per gram of tissue observed in splenic tissue. However, gold traces were not observed in the liver or kidney (Fig 5D). In human samples, HER2-positive breast tumors had a higher concentration of gold (22 µg/g of gold per tissue, $P = .039$) compared with HER2-negative TNBC tumors (8 µg/g of gold per tissue) (Fig 5E).

Discussion

Currently existing mammographic screening methods have several major drawbacks, such as exposure to ionizing radiation and/or insufficient sensitivity in younger populations with radiographically dense breasts or patients with postradiation fibrosis (8,42). Even when combined with US or MRI, mammography may still have nonspecific or false-positive results (8,42). Similarly, identification of residual fluorescence from

injected indocyanine green in a tumoral bed after the surgical removal of a tumor (1) and the reduced specificity to discriminate between benign and malignant sentinel lymph nodes (43) highlight the need for active targeting to accurately identify negative tumor margins during breast-conserving surgery. Thus, development of tumor-specific breast imaging tools represents an unmet medical need. MSOT imaging of the complex molecular phenotypes in cancers provides tunable modalities capable of detecting multiple parameters while ensuring maximal sensitivity. Promising advances in nanomedicine have established the ability of contrast agents to optoacoustically depict or treat breast cancers (1–3,6,7,13,14). However, to our knowledge, multiple clinically feasible and spectrally distinct contrast agents that can help detect heterogeneous tumor receptors simultaneously have not been reported (9–16). Thus, simultaneous use of multiple contrast agents has been limited because of an inability to dynamically measure two contrast agents at one time. Our study demonstrates the ability to detect and measure two distinct exogenous reporters using MSOT.

In this study, we found that HER2-expressing human breast cancers actively retained both TRA-Aurelia-1 and 2. However, HER2-negative TNBC tumors had negligible absorption of TRA-Aurelia-1 and 2 GNRs (Table, Fig 4A–4D). MSOT findings can provide a three-dimensional analysis of HER2 within the margins of HER2-positive cancers, representing a model to identify cancer-positive margins as MSOT depiction of HER2

margins indicates infiltration of the margins of HER2-expressing cancers by HER2-positive cancer cells. There is currently no similar model of HER2-negative cancers. A clinically similar model of positive margins based on MSOT depiction of phenotypic expression of a different uniquely expressed antigen could be developed. Thus, identification of positive margins with MSOT findings has great potential in similarly contributing to breast-conserving therapy with specific negative margins for successful image-guided surgery.

Aurelia-1 and Aurelia-2 GNRs have distinct optoacoustic spectra that can be separately and simultaneously identified using MSOT imaging. This study builds upon previous work on the identification of vascular patterns of human breast lesions based on single wavelength optoacoustic imaging (14) and demonstrates the successful, simultaneous detection of two exogenous, targeted reporters using MSOT, potentially allowing for the identification of multiplexed imaging. Our study also demonstrates that TRA-Aurelia-1 and TRA-Aurelia-2 GNRs were selective for HER2-expressing DY36T2Q orthotopic tumors in vivo and had a significantly increased optoacoustic signal in small tumors compared with MDA-MB-231 (HER2-negative) tumors (Fig 3A, 3B). These data were confirmed (Fig 5) using ICP-MS. TRA-Aurelia-1 and 2 GNR-enhanced MSOT-based simultaneous imaging uniquely offers a nonionizing method to detect HER2-positive cell populations with high sensitivity and relatively high resolution.

We further validated the selective retention and multispectral identification of TRA-Aurelia-1 and 2 in HER2-expressing human breast tumor tissues that were freshly resected (Fig 4A–4D). In the clinic, findings from imaging techniques such as radiography, intraoperative US, and optical spectroscopy are not currently sensitive enough to accurately predict the margins of resected breast tumors to guide surgery. Clinical MSOT systems can image at depths of about 5 cm (9); thus, future work should establish how many HER2-expressing cells can be detected at specific depths in larger animal models (eg, rats and pigs) and in humans.

The major limitation of the current study was that we utilized the same targeting strategy (TRA) that uses either Aurelia-1 or Aurelia-2 to determine the potential of MSOT findings to identify multiple reporters simultaneously. Additionally, the TRA targets a single domain IV of HER2 receptor. However, additional conjugation with pertuzumab that can specifically bind to domain II of the HER2 receptor could have further improved the diagnostic potential of Aurelia-1 and Aurelia-2 GNRs at MSOT imaging. To overcome these limitations, further studies with more rigorous study designs to target multiple domains of the HER2 receptors are warranted to improve the diagnostic potential for clinical applications.

In conclusion, the potent multispectral abilities of TRA-Aurelia-1 and TRA-Aurelia-2 were observed via optoacoustic imaging of both orthotopically implanted HER2-positive breast tumors (in vivo) and surgically resected HER2-positive breast tumor tissues (ex vivo). Most importantly, our results show that antibody conjugated GNRs allow for simultaneous, accurate detection of multiple colocalized GNRs in breast tumor tissue, creating a framework for the future clinical translation of this

imaging technique. MSOT imaging of GNRs is a unique, clinically feasible imaging technology that can simultaneously depict heterogeneous tumor signatures, thus allowing clinicians to rapidly implement the most appropriate therapeutic strategies and improve the efficacy of cancer treatments.

Acknowledgments: The authors would like to acknowledge Richey M. Davis, PhD, Virginia Tech University, for assistance in developing the ICP-MS experimental protocols and the support of Indrajeet Sharma, PhD, Department of Chemistry, University of Oklahoma, for the FTIR analysis.

Author contributions: Guarantors of integrity of entire study, **A.S., L.M., L.R.M.**; study concepts/study design or data acquisition or data analysis/interpretation, all authors; manuscript drafting or manuscript revision for important intellectual content, all authors; approval of final version of submitted manuscript, all authors; agrees to ensure any questions related to the work are appropriately resolved, all authors; literature research, **A.S., J.H., M.C.T., W.E.G., L.R.M.**; clinical studies, **A.S., A.T.**; experimental studies, **A.S., K.N.T., M.M., J.H., L.M., B.B., Y.Z., M.C.T., L.R.M.**; statistical analysis, **A.S., K.N.T., B.B., T.G., Z.S., L.R.M.**; and manuscript editing, **A.S., K.N.T., M.M., A.C., A.T., B.B., J.C.C.S., C.H., T.G., W.E.G., L.R.M.**

Disclosures of conflicts of interest: **A.S.** No relevant relationships. **K.N.S.** Grant from National Cancer Institute (grant no. R01CA205941, R01CA21350, P30). **M.M.** No relevant relationships. **J.H.** No relevant relationships. **A.C.** No relevant relationships. **A.T.** Funding from the Williams Family Chair in Breast Oncology; grant from Merck and Sanofi to institution; royalties from UpToDate paid to husband; consulting fees from Genentech, Eli Lilly and Company, and AstraZeneca; board member for BeyondSpring; stock or stock options from Johnson & Johnson, Pfizer, Merck, Gilead Sciences; Bristol Myers Squibb; and Doximity. **L.M.** No relevant relationships. **B.B.** Institutional support for the purchase of consumables. **Y.Z.** No relevant relationships. **M.C.T.** No relevant relationships. **J.C.C.S.** No relevant relationships. **C.H.** Medical advisory board member for EMD Serona; support from the ACRO to attend and speak at the ACRO Annual Meeting 2023; member of the Stephenson Cancer Center Data and Safety Monitoring Committee; co-chair of the Young Investigators Committee of the Head and Neck Cancer International Group. **T.G.** No relevant relationships. **Z.S.** No relevant relationships. **W.E.G.** U54 grant from National Cancer Institute. **L.R.M.** Grants from National Cancer Institute (grant no. R01CA205941, R01CA21350, P30CA225520, U54CA118948), OU Surgery Research Fund (OUCARES), the V.V. Cooke Foundation, and the Williams Family Chair in Breast Oncology; payments from the Radiological Society of North America for deputy editorial duties for *Radiology: Imaging Cancer*.

References

1. Pop FC, Veys I, Vankerckhove S, et al. Absence of residual fluorescence in the surgical bed at near-infrared fluorescence imaging predicts negative margins at final pathology in patients treated with breast-conserving surgery for breast cancer. *Eur J Surg Oncol* 2021;47(2):269–275.
2. St John ER, Al-Khudairi R, Ashrafian H, et al. Diagnostic Accuracy of Intraoperative Techniques for Margin Assessment in Breast Cancer Surgery: A Meta-analysis. *Ann Surg* 2017;265(2):300–310.
3. Tang SS, Kaptanis S, Haddow JB, et al. Current margin practice and effect on re-excision rates following the publication of the SSO-ASTRO consensus and ABS consensus guidelines: a national prospective study of 2858 women undergoing breast-conserving therapy in the UK and Ireland. *Eur J Cancer* 2017;84:315–324.
4. Thomas A, Rhoads A, Suhl J, et al. Incidence and Survival by Human Epidermal Growth Factor Receptor 2 Status in Young Women With Stage I-III Breast Cancer: SEER, 2010–2016. *Clin Breast Cancer* 2020;20(4):e410–e422.
5. Thomas A, Rhoads A, Pinkerton E, et al. Incidence and Survival Among Young Women With Stage I-III Breast Cancer: SEER 2000–2015. *JNCI Cancer Spectr* 2019;3(3):pkz040.
6. Pleijhuis RG, Graafland M, de Vries J, Bart J, de Jong JS, van Dam GM. Obtaining adequate surgical margins in breast-conserving therapy for patients with early-stage breast cancer: current modalities and future directions. *Ann Surg Oncol* 2009;16(10):2717–2730.
7. Sosin M, Gupta SS, Wang JS, et al. A Prospective Analysis of Quality of Life and Toxicity Outcomes in Treating Early Breast Cancer With Breast Conservation Therapy and Intraoperative Radiation Therapy. *Front Oncol* 2018;8:545.
8. Miller B, Chalfant H, Thomas A, et al. Diabetes, Obesity, and Inflammation: Impact on Clinical and Radiographic Features of Breast Cancer. *Int J Mol Sci* 2021;22(5):2757.

9. MacCuaig WM, Jones MA, Abeyakoon O, McNally LR. Development of Multispectral Optoacoustic Tomography as a Clinically Translatable Modality for Cancer Imaging. *Radiol Imaging Cancer* 2020;2(6):e200066.
10. McNally LR, Mezera M, Morgan DE, et al. Current and Emerging Clinical Applications of Multispectral Optoacoustic Tomography (MSOT) in Oncology. *Clin Cancer Res* 2016;22(14):3432–3439.
11. Regensburger AP, Fonteyne LM, Jüngert J, et al. Detection of collagens by multispectral optoacoustic tomography as an imaging biomarker for Duchenne muscular dystrophy. *Nat Med* 2019;25(12):1905–1915.
12. Knieling F, Neufert C, Hartmann A, et al. Multispectral Optoacoustic Tomography for Assessment of Crohn's Disease Activity. *N Engl J Med* 2017;376(13):1292–1294.
13. Diot G, Metz S, Noske A, et al. Multispectral Optoacoustic Tomography (MSOT) of Human Breast Cancer. *Clin Cancer Res* 2017;23(22):6912–6922.
14. Abeyakoon O, Morscher S, Dalhaus N, et al. Optoacoustic Imaging Detects Hormone-Related Physiological Changes of Breast Parenchyma. *Ultraschall Med* 2019;40(6):757–763.
15. Bhutiani N, Samykutty A, McMasters KM, Egilmez NK, McNally LR. In vivo tracking of orally-administered particles within the gastrointestinal tract of murine models using multispectral optoacoustic tomography. *Photoacoustics* 2018;13:46–52.
16. Harold KM, MacCuaig WM, Holter-Charkabarty J, et al. Advances in Imaging of Inflammation, Fibrosis, and Cancer in the Gastrointestinal Tract. *Int J Mol Sci* 2022;23(24):16109.
17. Hupple CW, Morscher S, Burton NC, Pagel MD, McNally LR, Cárdenas-Rodríguez J. A light-fluence-independent method for the quantitative analysis of dynamic contrast-enhanced multispectral optoacoustic tomography (DCE MSOT). *Photoacoustics* 2018;10:54–64.
18. Xiao TG, Weis JA, Gayzik FS, et al. Applying dynamic contrast enhanced MSOT imaging to intratumoral pharmacokinetic modeling. *Photoacoustics* 2018;11:28–35.
19. Zeiderman MR, Morgan DE, Christein JD, Grizzle WE, McMasters KM, McNally LR. Acidic pH-targeted chitosan capped mesoporous silica coated gold nanorods facilitate detection of pancreatic tumors via multispectral optoacoustic tomography. *ACS Biomater Sci Eng* 2016;2(7):1108–1120.
20. Gurka MK, Pender D, Chuong P, et al. Identification of pancreatic tumors in vivo with ligand-targeted, pH responsive mesoporous silica nanoparticles by multispectral optoacoustic tomography. *J Control Release* 2016;231:60–67.
21. Yin W, Kimbrough CW, Gomez-Gutierrez JG, et al. Tumor specific liposomes improve detection of pancreatic adenocarcinoma in vivo using optoacoustic tomography. *J Nanobiotechnology* 2015;13(1):90.
22. Thomas A, Samykutty A, Gomez-Gutierrez JG, et al. Actively Targeted Nanodelivery of Echinomycin Induces Autophagy-Mediated Death in Chemoresistant Pancreatic Cancer In Vivo. *Cancers (Basel)* 2020;12(8):2279.
23. Becker A, Masthoff M, Claussen J, et al. Multispectral optoacoustic tomography of the human breast: characterisation of healthy tissue and malignant lesions using a hybrid ultrasound-optoacoustic approach. *Eur Radiol* 2018;28(2):602–609.
24. Goh Y, Balasundaram G, Moothanchery M, et al. Multispectral Optoacoustic Tomography in Assessment of Breast Tumor Margins During Breast-Conserving Surgery: A First-in-human Case Study. *Clin Breast Cancer* 2018;18(6):e1247–e1250.
25. Paprotski RJ, Li Y, Barber Q, Lewis JD, Campbell RE, Zemp R. Validating tyrosinase homologue melA as a photoacoustic reporter gene for imaging *Escherichia coli*. *J Biomed Opt* 2015;20(10):106008.
26. Wagner AL, Danko V, Federle A, et al. Precision of handheld multispectral optoacoustic tomography for muscle imaging. *Photoacoustics* 2020;21:100220.
27. Bae YH. Drug targeting and tumor heterogeneity. *J Control Release* 2009;133(1):2–3.
28. Hobbs SK, Monsky WL, Yuan F, et al. Regulation of transport pathways in tumor vessels: role of tumor type and microenvironment. *Proc Natl Acad Sci USA* 1998;95(8):4607–4612.
29. Jackson CT, Jeong S, Dorlhiac GF, Landry MP. Advances in engineering near-infrared luminescent materials. *iScience* 2021;24(3):102156.
30. Yim W, Zhou J, Mantri Y, Creyer MN, Moore CA, Jokerst JV. Gold Nanorod-Melanin Hybrids for Enhanced and Prolonged Photoacoustic Imaging in the Near-Infrared-II Window. *ACS Appl Mater Interfaces* 2021;13(13):14974–14984.
31. Sanders M. A review of controlled clinical trials examining the effects of antimalarial compounds and gold compounds on radiographic progression in rheumatoid arthritis. *J Rheumatol* 2000;27(2):523–529.
32. Libutti SK, Paciotti GF, Byrnes AA, et al. Phase I and pharmacokinetic studies of CYT-6091, a novel PEGylated colloidal gold-rhTNF nanomedicine. *Clin Cancer Res* 2010;16(24):6139–6149.
33. Kharlamov AN, Tyurnina AE, Veselova VS, Kovtun OP, Shur VY, Gabinsky JL. Silica-gold nanoparticles for atheroprotective management of plaques: results of the NANOM-FIM trial. *Nanoscale* 2015;7(17):8003–8015.
34. Xu D, Mao JC, He Y, Yeung ES. Size-tunable synthesis of high-quality gold nanorods under basic conditions by using H₂O₂ as the reducing agent. *J Mater Chem C Mater* 2014;2(25):4989–4996.
35. Khanal A, Ullum C, Kimbrough CW, et al. Tumor targeted mesoporous silica-coated gold nanorods facilitate detection of pancreatic tumors using Multispectral optoacoustic tomography. *Nano Res* 2015;8(12):3864–3877.
36. Samykutty A, Grizzle WE, Fouts BL, et al. Optoacoustic imaging identifies ovarian cancer using a microenvironment targeted theranostic wormhole mesoporous silica nanoparticle. *Biomaterials* 2018;182:114–126.
37. Repetto G, del Peso A, Zurita JL. Neutral red uptake assay for the estimation of cell viability/cytotoxicity. *Nat Protoc* 2008;3(7):1125–1131.
38. Gomez-Gutierrez JG, Bhutiani N, McNally MW, et al. The neutral red assay can be used to evaluate cell viability during autophagy or in an acidic microenvironment in vitro. *Biotech Histochem* 2021;96(4):302–310.
39. MacCuaig WM, Fouts BL, McNally MW, et al. Active Targeting Significantly Outperforms Nanoparticle Size in Facilitating Tumor-Specific Uptake in Orthotopic Pancreatic Cancer. *ACS Appl Mater Interfaces* 2021;13(42):49614–49630.
40. Borovjagin AV, McNally LR, Wang M, Curiel DT, MacDougall MJ, Zinn KR. Noninvasive monitoring of mRFP1- and mCherry-labeled oncolytic adenoviruses in an orthotopic breast cancer model by spectral imaging. *Mol Imaging* 2010;9(2):59–75.
41. Kimbrough CW, Khanal A, Zeiderman M, et al. Targeting Acidity in Pancreatic Adenocarcinoma: Multispectral Optoacoustic Tomography Detects pH-Low Insertion Peptide Probes In Vivo. *Clin Cancer Res* 2015;21(20):4576–4585.
42. Deán-Ben XL, Fehm TF, Gostic M, Razansky D. Volumetric hand-held optoacoustic angiography as a tool for real-time screening of dense breast. *J Biophotonics* 2016;9(3):253–259.
43. Pop CF, Veys I, Gomez Galdon M, et al. Ex vivo indocyanine green fluorescence imaging for the detection of lymph node involvement in advanced-stage ovarian cancer. *J Surg Oncol* 2018;118(7):1163–1169.